ADVANCED MATERIALS INTERFACES Open Access
www.advmatinterfaces.de

Reconfigurable Soft Actuators Constructed via Layer-by-layer Assembly

Qing Chen, Loghman Jamilpanah, Tina Künniger, Roman Furrer, Qun Song, Kai Zhang, Andrei Chumakov, Constantin Harder, Yusuf Bulut, Peter Müller-Buschbaum, Stephan V. Roth, and Artur Braun**

Stimuli-responsive actuators are candidates for the development of soft robots due to their shape deformation and environmental adaptation capabilities. Adaptation to environmental stimuli not only enables complex shape reprogramming but also benefits the recovery of mechanical injuries of the soft actuators. Nevertheless, reports on soft actuators that integrate shape-reprogramming and injury-healing functions into a monolithic actuating material through facile fabrication strategies remain scarce. Herein, a stimuli-responsive and healable actuator is developed via layer-by-layer casting of two stimuli-responsive materials with complementary properties. Upon specific stimulation, these two materials reorganize their structural network at the nano- and microscales and heal. The resulting actuator exhibits a robust photo-responsive actuating strength due to the asymmetric volumetric responses of the two layers. Importantly, the whole actuator can be healed with the aid of a sequential heating-humidifying–drying treatment, achieving excellent healing efficiency in both mechanical strength (72%) and actuating strength (95%). Moreover, the initial actuation modes can be restored and diversified through humidifying or heating-assisted welding procedures, respectively. This work demonstrates a facile strategy to construct reprogrammable actuators with healing and welding abilities stimulated by two environmental stimuli and provides a platform for developing adaptable materials to a changing environment.

1. Introduction

The ability of detecting and adapting to environmental changes is of vital importance to the survival of living organisms.[1] Inspired by nature, soft actuators are developed utilizing structurally programmable or comfortable materials, which are capable of converting the energy from environmental stimuli into reversible shape deformation and locomotion.[2,3] Based on these materials, soft actuators have attracted significant attention in the fields of soft robotics,[4] bionics,[5] and smart materials.[6]

The stable actuating performance and mechanical property are the prerequisites for the long-term stability of soft actuators.[7] Therefore, the capability of healing or repairing is highly desired for the restoration of the soft actuators after severe mechanical damage.[8] Except for improving the durability of actuators, the healing ability also enables reconfiguring of the actuators and diversifying

---

Q. Chen
Spallation Neutron Source Science Center
Dongguan 523803, China
E-mail: chenqing@ihep.ac.cn

Q. Chen
Institute of High Energy Physics
Chinese Academy of Science
Beijing 100049, China

Q. Chen, L. Jamilpanah, A. Braun
Laboratory for High Performance Ceramics
Empa
Swiss Federal Laboratories for Materials Science and Technology
Dübendorf 8600, Switzerland
E-mail: artur.braun@alumni.ethz.ch

The ORCID identification number(s) for the author(s) of this article can be found under https://doi.org/10.1002/admi.202500269

DOI: 10.1002/admi.202500269

T. Künniger
Cellulose and Wood Materials
Empa
Swiss Federal Laboratories for Materials Science and Technology
Dübendorf 8600, Switzerland

Q. Song, K. Zhang
Sustainable Materials and Chemistry
Dept. Wood Technology and Wood-based Composites
University of Göttingen
37077 Göttingen, Germany

R. Furrer
Transport at Nanoscale Interfaces Laboratory
Empa
Swiss Federal Laboratories for Materials Science and Technology
Dübendorf 8600, Switzerland

L. Jamilpanah
Magnetic and Functional Thin Films Laboratory
Empa
Swiss Federal Laboratories for Materials Science and Technology
Dübendorf 8600, Switzerland

A. Chumakov, C. Harder, Y. Bulut, S. V. Roth
Deutsches Elektronen-Synchrotron
Notkestrasse 85, 22607 Hamburg, Germany

the deformation modes through welding or re-assembling of the actuators.[9] Thus, there is an increasing demand for developing healable materials, in order to prepare these soft actuating systems for adaptive and durable applications in harsh environments.[10] However, it remains a challenge to incorporate stimuli-responsive actuating and healing capabilities into one actuator on the same material basis.

Extensive structural design strategies have been developed to tackle the challenge above. A rational organization of several functional material elements is of great significance. The first strategy to design healable actuators with a single-layer geometry is to employ dynamic crosslinking mechanisms, such as hydrogen bonding,[11] supramolecular cross-linking,[12] and other dynamic non-covalent,[13] as well as covalent bonds,[3,14] or their combinations.[15] In this strategy, the single-layered material normally features an anisotropic structure either in the in-plane or out-of-plane directions. However, most single-layered actuators based on anisotropic-structured thin films usually suffer from monotonous actuating modes.[16]

The second strategy is to design healable actuators with a double- or multi-layered geometry. In this strategy, the anisotropic structures are formed only in the out-of-plane direction among the layers. Indeed, Chen et al. assembled an ink/polyurethane double-layered actuator maintained by hydrogen-bonding interactions, which achieved a water-assisted healing and light-responsive actuating performance.[17] Ge et al. designed a tri-layered actuator with dual-responsiveness to humidity and temperature, and also a healing ability assisted with water.[18] Moreover, Ji et al. developed a carbonized silk fabric (CSF)-vitrimer bi-layered actuator with not only responsiveness to but also healability triggered by multiple stimuli.[19] Despite these great achievements, the development of double-or multi-layered healable actuators usually involves elaborate designs and complex fabrication procedures, since it requires each constituent layer 1) to be healable, 2) to undergo different volumetric responses upon stimulation to achieve actuation function,[20] and 3) to form a strong interface among each other for maintaining the integrity of the device.[21] Therefore, the quest for developing healable actuators with a simple design and cost-effective fabrication approach is ever-increasing.

In this work, we constructed a bi-layered (BL) actuator with both stimuli-responsive actuating and healing capabilities. Using the layer-by-layer (LBL) casting strategy, a humidity-responsive and a thermal-responsive thin film with excellent actuating and healing functions are laminated to construct a BL actuator. LBL is a well-established method for constructing functional composites with hierarchical structure.[22] The as-obtained actuator deforms under infrared light irradiation. Moreover, a punctured BL actuator can be healed through a sequentially heating and humidifying treatment. In addition, the structural rearrangement of the two constituent layers also enables the actuator to be reprogrammed into diverse actuation modes by welding the two layers, which achieves complex deformation modes unattainable by unwelded actuators. In general, we realized functional integration and engineering implementation of a prototype of healable actuators. The actuating, healing, and welding functions of this actuator make it a promising candidate for the development of next-generation intelligent devices.

2. Results and Discussion

2.1. Design and Fabrication of the BL Actuator

2.1.1. Designing the Constituent Layers

We organized two stimuli-responsive and structural-programmable materials with complementary properties into one bi-layered (BL) actuator to accommodate the stimuli-responsiveness of each constituent layer. The two constituent layers were prepared by the casting of the mixed solution of the respective material elements. The humidity-responsive layer is fabricated by embedding a rigid scaffold polymer into a soft matrix polymer. Poly(3,4-ethylenedioxythiophene):poly(styrene sulfonate) (PEDOT:PSS) and carboxymethyl cellulose (CMC) are used as the scaffold and matrix due to their humidity-responsive actuating and self-healing performance, respectively.[23] The supramolecular network forms via H-bonding and electrostatic interactions between CMC and PEDOT:PSS in this material, which is described as "PPC film" in the following manuscript (**Figure 1a**).

The thermal-responsive layer is designed by incorporating Fe_3O_4 nanoparticles (NPs) into a functionalized polydimethylsiloxane (PDMS) matrix sustained by synergetic supramolecular interactions. Fe_3O_4 NPs are expected to act as photo-thermal fillers and silylated cellulose nanocrystal (Si-CNC) was used to construct the dynamic network of the matrix to adapt both hydrophobic interactions with PDMS and hydrogen bonding with the neighboring molecules and give access to structural rearrangement.[24] We call it "MCP film" in the following parts of the manuscript. It should be emphasized that the two constituent materials have been demonstrated with excellent actuating and healing functions under a humidifying–drying and a heating–cooling treatment, respectively, which originates from the nano- and micro-scale restructuring of these materials triggered by their specific stimulus.

Subsequently, the PPC and MCP films are laminated via layer-by-layer assembly and form a BL actuator through oxygen plasma treatment of the MCP film followed by drop casting of the PPC film (Figure 1a). The thickness ratio of the actuator is fixed at 10:1 throughout this work. The dynamic and non-covalent crosslinking (H-bonding) is employed as the molecular basis for the structural rearrangement of the supramolecular network of the stimuli-responsive polymers, and also the binder for interfacial bonding across the layers to maintain the integrity of the bilayer.

C. Harder, Y. Bulut, P. Müller-Buschbaum
TUM School of Natural Sciences
Department of Physics
Technical University of Munich
85748 Garching, Germany

S. V. Roth
Department of Fiber and Polymer Technology
KTH Royal Institute of Technology
Stockholm 10044, Sweden

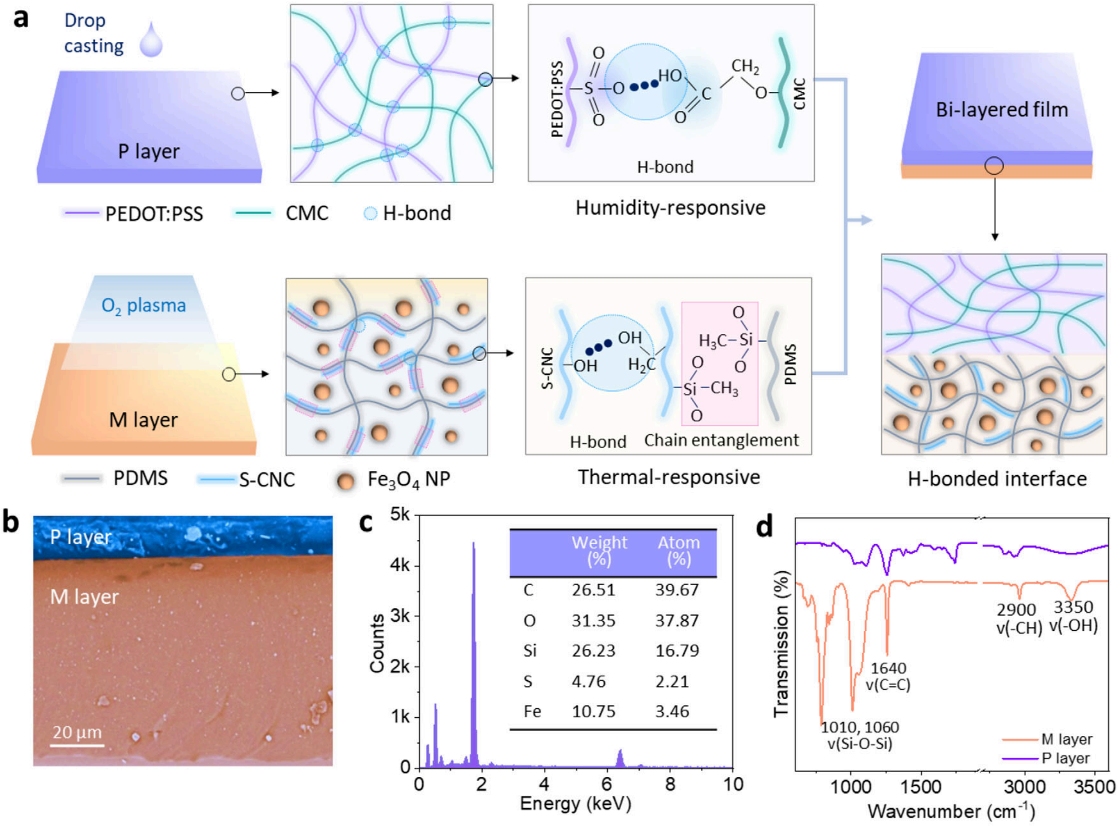

Figure 1. Formation of the bi-layered (BL) film comprising the PEDOT:PSS/CMC (PPC film) and the Fe_3O_4NP/Si-CNC/PDMS (MCP film). a) Layer-by-layer deposition of the BL actuator. b,c) Cross-sectional SEM micrograph and EDS examination of the BL film. d) FTIR spectrum of the PPC film and the MCP film.

2.1.2. Morphological and Compositional Analysis of the Bi-Layer

At the cross-section scanning electron microscopy (SEM) micrographs of the BL film (Figure 1b), the PPC film (blue) can be clearly distinguished from the MCP film (brown). The upper part (PPC film) exhibits a lamellae architecture with interconnected fibrils and pores. These pores can participate in the transient H-bonding interactions with and mass transfer of water molecules, which provides the basis for humidity-responsive actuation. The lower part of the SEM micrographs (MCP film) shows a relatively smooth and uniform morphology as compared to the PPC film. The morphology of the MCP film is mainly composed of ordered Fe_3O_4 NP assemblies with a diameter of less than 160 nm connected and surrounded by a polymer matrix (Figure S1, Supporting Information). The low agglomeration rate of Fe_3O_4 NPs might be due to the richness in functional groups of Si-CNC and is expected to endow the nanocomposites with excellent photothermal conversion efficiency. It can be clearly seen that two layers are closely bonded at the interface without any indication of delamination. In Figure 1c, the energy-dispersive X-ray spectroscopy (EDS) analysis indicates a relatively sharp distribution of Si element and a smooth and uniform distribution of Fe element.

Fourier-transform infrared (FTIR) spectroscopy is performed to identify the chemical crosslinking of the two constituent layers. The PPC film shows a strong characteristic peak of the —OH stretching vibration at 3344 cm^{-1}, suggesting a dense hydrogen bonding network, which is necessary for its effective interaction with water. From the FTIR spectra of the MCP film, we observe both the methyl siloxy groups at 1261 cm^{-1} and hydroxyl groups at 3350 cm^{-1} (Figure 1d). This suggests that Si-CNC could participate in constructing the dynamic network of the MCP film through both hydrophobic interactions between silylated cellulose and PDMS, as well as hydroxyl groups for H-bonding and physical entanglements with the neighboring molecules.

2.2. Stimuli-Responsive Properties of the PPC and MCP Films

2.2.1. The Structural Basis of Stimuli Responsiveness

To study the structural basis of the stimuli-sensitivity of the two films, small-angle scattering (SAS) experiments are performed, including small-angle X-ray scattering (SAXS) and small-angle neutron scattering (SANS) (Figure S2, Supporting Information). Since the heat-conducting ability of the MCP film highly depends on the radii of Fe_3O_4 NP assemblies and their inter-particle distances, we decipher the structure of Fe_3O_4 NP assemblies through the fitting of the SAS data. Both the SAXS and SANS curves reveal that the scattering pattern of the BL film is the combination of the signals of the constituent layers (**Figure** 2a,b).

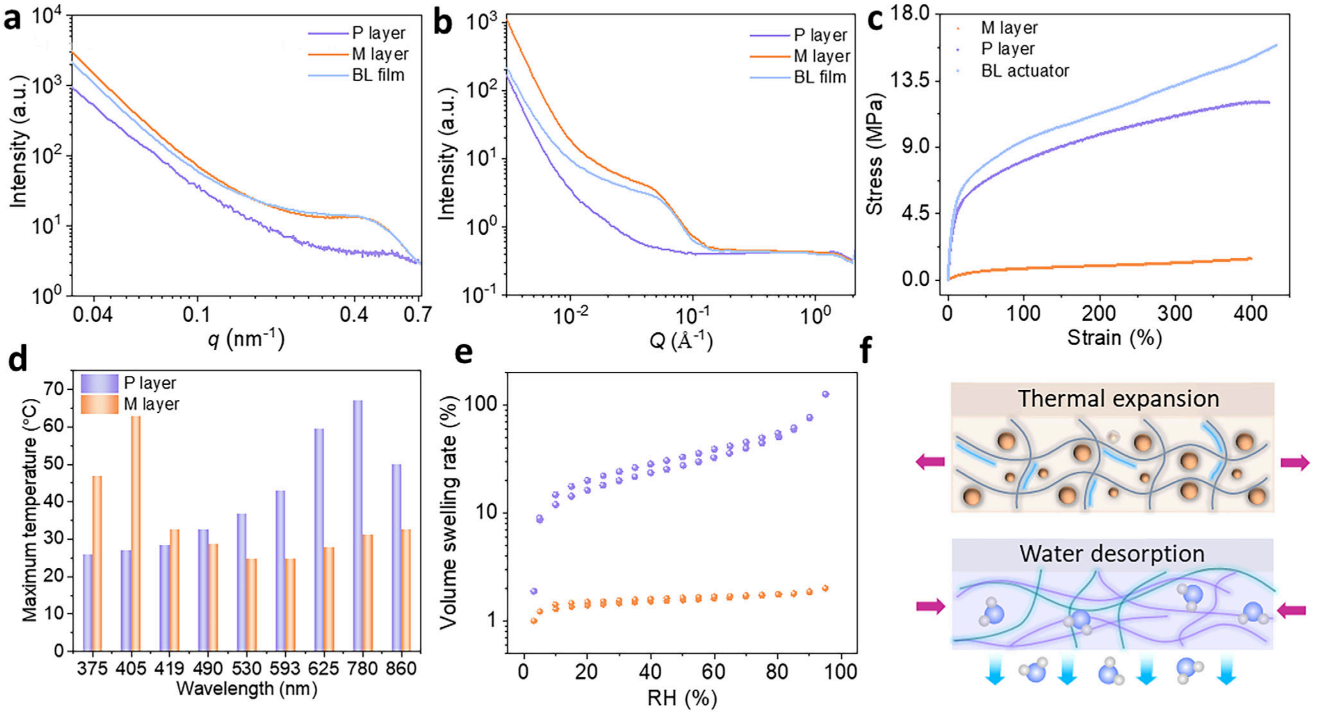

Figure 2. Small-angle scattering analysis of the actuator, and the stimuli-responsiveness of the constituent layers. a,b) SAXS and SANS patterns of the PPC, MCP, and bi-layered films, respectively. c) Comparison of the strain–stress curves of the PPC, MCP, and the bi-layered films. d) Temperature at maximum of the PPC and MCP films when being illuminated by LEDs at different wavelengths at the power density of 78 mW cm^{-2}. e) Dynamic vapor sorption analysis of the PPC film and MCP film. f) Schematic mechanism of the photo-responsiveness of the BL actuator.

The fitting is performed using a combined structural model proposed in our previous work, which is composed of a core–shell sphere to represent the large Fe_3O_4 NP agglomerates, a cylinder to represent the polymer matrix and a sphere for small Fe_3O_4 NP clusters.[24]

The radii of the core from fitting are $R_{core} = 84.0 \pm 6.7$ nm from SAXS and $R_{core} = 89.0 \pm 8.5$ nm from SANS, and the thickness of the shell are $\sigma_{shell} = 46 \pm 4$ nm from SAXS and 44 ± 4 nm from SANS, respectively (Figure S3, Supporting Information). The difference between the fit parameters from SAXS and SANS may originate from the ratio between the scattering length densities of Fe_3O_4 and that of the Si-CNC/PDMS matrix in neutron and X-ray scattering (Table S1, Supporting Information). The large NP agglomerates and small NP clusters combine and form a closely-packed network, which is beneficial for photo-thermal energy conversion and the actuating performance of the actuator.

Moreover, the mechanical properties of the two respective layers and the bi-layered film are compared. The PPC film features excellent mechanical properties, with a tensile strength of 11.89 MPa and a fracture strain of 426% (Figure 2c). This could be attributed to the densely-packed lamellar structure and multiple H-bonded networks. The MCP film is highly elastic, and shows a maximum strength and elongation-at-break of 1.45 MPa and 397%, respectively. The tensile strain–stress curve of the bi-layered film suggests that the mechanical behavior of the bilayer is the combination of the properties of the two monolayers. The high tensile strength of the PPC film and the elasticity of the MCP film are beneficial for the reversibility and reliability of the bending deformation of the BL actuator.

Furthermore, we investigate the UV/vis absorption spectra of the water dispersion of Fe_3O_4 NPs and PEDOT:PSS since the other components (CMC and S-CNC/PDMS) are transparent and their absorption is negligible. The PEDOT:PSS dispersion shows a broad absorption range from the UV (300 nm) to infrared (IR, 900 nm) with a peak centering at 860 nm, while the absorption peak of Fe_3O_4 NPs is relatively sharp at 380 nm and is nearly flat in the IR range (Figure S4, Supporting Information). Besides, IR light has a stronger photo-thermal effect as well as a deeper penetration than short-wavelength light and is widely used in photo-heating. Therefore, we used either an IR LED ($\lambda = 780$ nm) or a UV LED ($\lambda = 375$ nm) as the light source to investigate the actuation performance of the BL actuator. Besides, an infrared camera is used to record the time-dependent temperature variations of the two constituent layers, respectively. The results suggest that the heating rates vary when the BL actuator is exposed to LEDs at different wavelengths (Figure 2d), which are generally in accordance with the trend that we observed in the spectra of UV/vis absorption (Figure S4, Supporting Information).

Therefore, the BL actuator can be activated under the thermal as well as photo stimuli due to the combined action of the photothermal conversion of the MCP film, the mechanical strength, and the difference in the thermal expansion degree between the PPC and MCP films. The PPC film features a negative thermal expansion coefficient (CTE) due to the volume shrinkage induced by water loss (Figure S5, Supporting Information). The volume shrinkage of the PPC film is induced by water desorption, which is demonstrated via dynamic vapor sorption analysis (Figure 2e).[23] On the contrary, PDMS typically have a positive

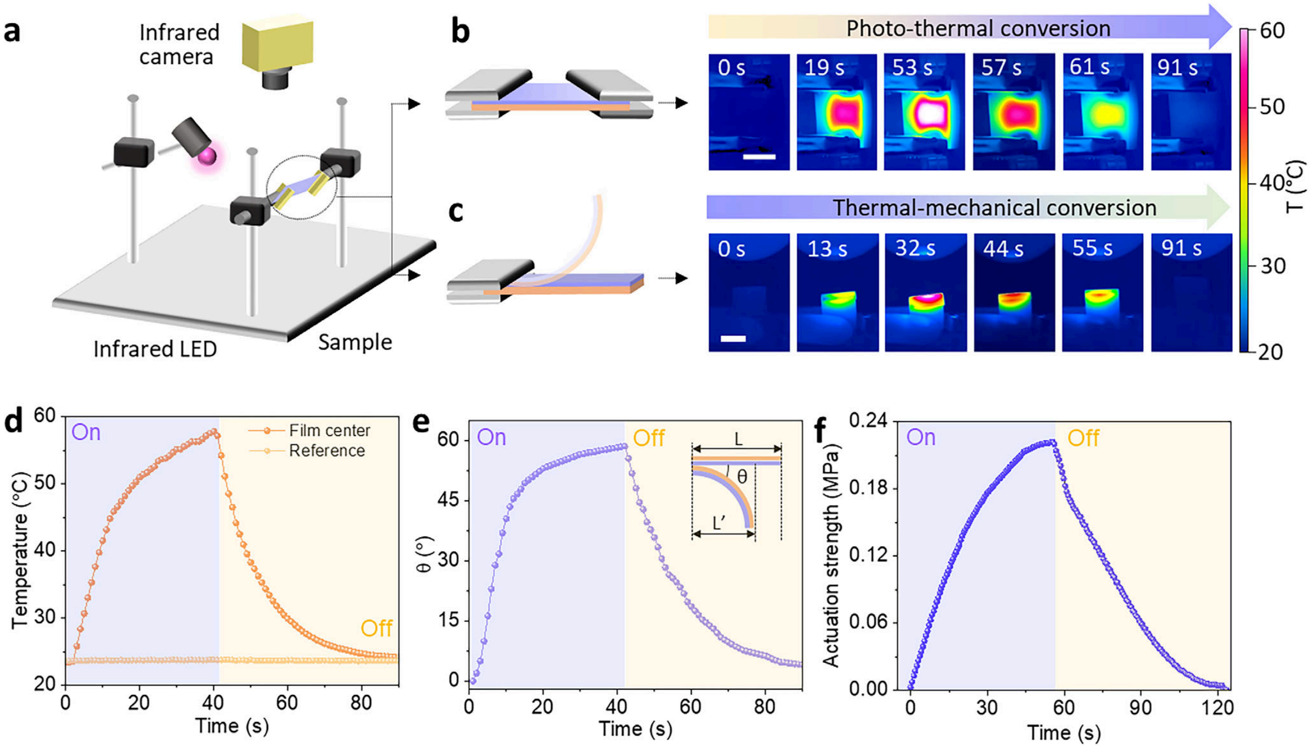

Figure 3. Photo-responsive actuation performance of the BL actuator. a) Schematic of the experimental setup for recording the temperature of the BL actuator when they are illuminated by an IR LED (wavelength: 780 nm, power density: 28 mW cm^{-2}) with an infrared camera. b) To visualize the photo-thermal response of the BL actuator, the sample is clamped at the two ends by holders. Right: The as-obtained thermal images show the temperature variation of a bi-layered actuator when the LED is switched on and off. During the process of photo-thermal conversion. c) To record the temperature and bending curvature of the film during thermal-mechanical conversion, the sample is clamped at only one end by the holder. Right: The as-obtained thermal images show the temperature variation and shape deformation during a photo-responsive bending/unbending cycle. d) Temperature of the BL actuator extracted from the thermal images in (b). e) The bending angle of the BL actuator is calculated from the length of the actuator in (c). f) The actuation force is recorded when the BL actuator is illuminated by an IR LED at the wavelength of 780 nm. The light is switched on to induce a contracting force to straighten the actuator, and then the light is turned off at the ambient condition for the film to swell and soften until the equilibrium state.

high CTE (300×10^{-6} °C^{-1}),[25] which results in a high CTE of the MCP film. The difference in thermal expansion degree leads to a strain mismatch at the layer-interfaces and the following thermal-responsive bending deformation. Benefiting from the water desorption from the PPC film and the heat dissipation from the MCP film, the BL actuator is proposed to perform bending/unbending deformation under the stimulation of light (Figure 2f).

2.2.2. Photo-Responsive Actuation of the BL Actuator

In the next part, we investigated the photo-thermo-mechanical response of the BL actuator. The photo-thermal response of the BL actuator is recorded by an infrared camera with the testing setup depicted in **Figure 3**a,b. LEDs are installed and connected with a Thorlab LED controller. The infrared camera is calibrated before the measurement (Figure S6, Table S2, Supporting Information). When the LED is switched on (λ = 780 nm, I = 78 mW cm^{-2}), the temperature at the center of the actuator rises from 22 to 67 °C (with a ΔT of 43 °C) in 53 s, and returns to the original state after 40 s (Figure 3b; Figure S7, Supporting Information). The higher power densities of the LED we use, the greater the temperature increase will be obtained due to the photo-thermal property of the MCP film (Figure S8, Supporting Information). The moderate photo-thermal conversion efficiency ensures the actuator with a stable and powerful IR actuating performance.

The photo-thermal-mechanical response of the BL actuator is investigated by the same experimental setup in Figure 3b with a slight modification: one sample holder of the actuator is removed, and the released free end of the actuator can deform under the illumination of IR LED (Figure 3c). The time-dependent variation of the surface temperature and bending angle of the BL actuator are studied and compared within one actuation cycle. For the variation of temperature, when the IR LED is switched on (λ = 780 nm, I = 78 mW cm^{-2}), the center of the actuator is heated to 58 °C in 40 s. When the LED is switched off, the irradiated region cools down to 24 °C in 40 s (Figure 3d; Movie S1, Supporting Information).

The bending angle (θ) of the BL actuator is calculated by the method described in Figure S9 (Supporting Information) as a function of time. The maximum bending angle of the BL actuator is 59° (Figure 3e; Figure S10, Supporting Information). It is observed that the actuator begins to bend and its temperature increases rapidly when the light is switched on, and gradually returns to the original state when the light is switched off. The

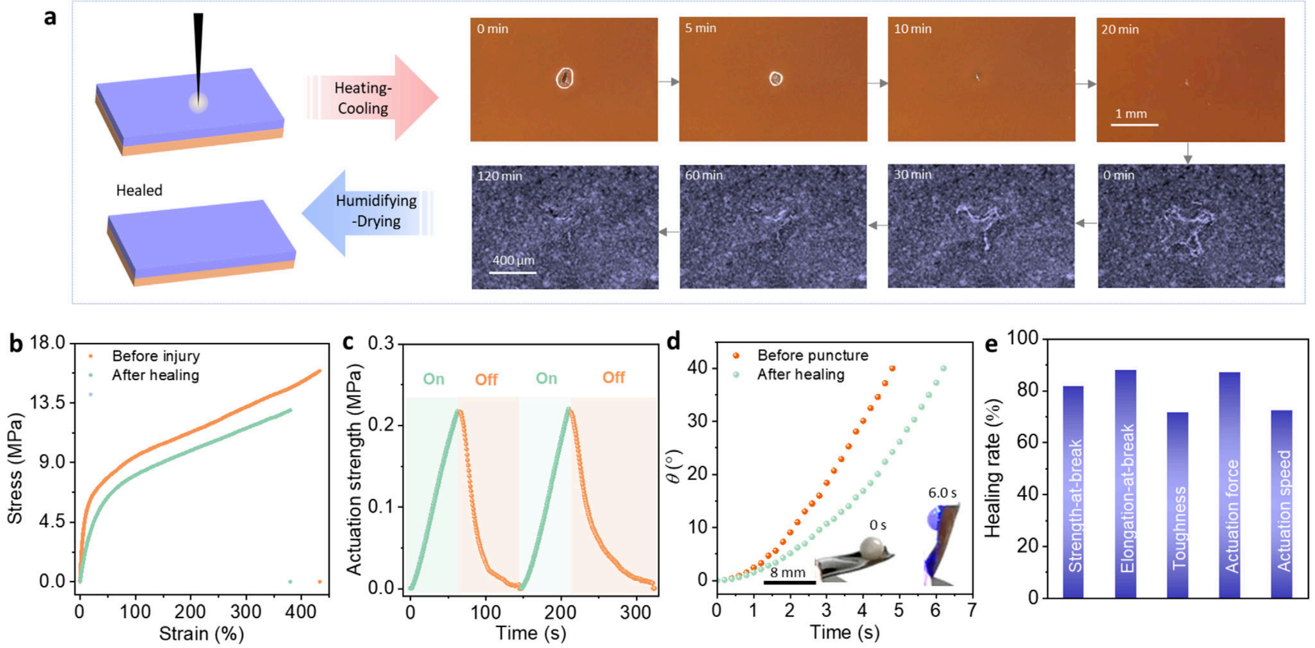

Figure 4. The healing performance of the BL actuator. a) Schematic diagram of the healing strategy for the BL actuator, with optical microscopic images depicting the healing process of the PPC and MCP films, respectively. b) Strain–stress curves of the BL actuator before injury and after healing. c) Actuation strength of the healed BL actuator. d) Time-dependent variation of the bending angle of the "sit-up" athlete based on the BL actuator before and after healing in response to UV LED. e) The healing performance of the BL actuator with respect to the strength-at-break, elongation-at-break, toughness, actuation force, and actuation speed calculated from the results in (b–d).

bending curvature and temperature of the actuator display a similar variation trend.

Meanwhile, the temperature field induced by the photothermal effect generates an actuation force. The light-induced actuating force under IR illumination is measured with a Zwick mechanical tester at the ambient condition (RH = 30%, T = 25 °C) using the setup as shown in Figure S11 (Supporting Information). An actuating force is generated when the LED is switched on, attaining its maximum at 0.23 MPa (tension), and dramatically decreases to zero by absorption of water vapor from the environment when the LED is switched off (relaxation, Figure 3f; Figure S10, Supporting Information). The actuating force originates from the instantaneous contraction of the PPC film and a sharp increase in its actuation strain due to the instant temperature gradient between the actuator and the environment. The light-induced actuation force of the BL actuator is comparable to the internal stress of animal muscles.[26]

2.3. Healing and Welding Functions Aided by Structural Rearrangement

Soft actuators are inevitably subjected to small microscale injuries and cracks during operation. Thus, the self-healing property is of vital importance for the actuators to maintain an extended service life. The recovery of the actuating function requires the restoration of both the structural and mechanical properties of the actuator. By in situ SAXS and dynamic mechanical analysis, our previous work indicates that both the thermal-responsive MCP film and the humidity-responsive PPC film are healable assisted by structural rearrangement (Figure S12, Supporting Information). Thus, we explored the potential of the stimuli-induced structural rearrangement of the two respective materials on the healing and welding abilities of the bi-layered actuator.

2.3.1. The Healing Phenomenon

The recovery of the BL actuator is examined by optical microscopy under successive heating and humidifying treatment. A strip of BL actuator (10 mm × 5 mm × 0.5 mm) is punctured through with a cross-shaped hole as the injury (diameter = 0.5 mm). **Figure 4a** reveals the morphologies at the two sides of the actuator, respectively.

When we heat the BL actuator near the T_m of the MCP film, the polymer matrix reorganizes through liquid–solid transition facilitated by heat conduction through Fe_3O_4 NP assemblies i). Thus, the punctured hole nearly vanished in the MCP film after heating at 60 °C for 0.5 h. Meanwhile, the widening of the injured area in the PPC film is observed, this is due to that heating also leads to volume shrinkage and broadening of the injury ii). Through the subsequent humidifying treatment, the supramolecular network in the PPC film becomes swollen and reattaches. Simultaneously, the cooling effect of moisture aids in the recovery of elastic properties of the MCP film since it's less vulnerable to moisture as indicated by FTIR iii). Therefore, the injury becomes almost invisible after the subsequent humidifying treatment (T = 25 °C, RH = 50%, 3 h). And the healing interface in the MCP film side is also negligible. Finally, the supramolecular network of the PPC film recovers in when the relative humidity returns to the ambient condition iv). The microscopic examinations demonstrate not only the recovery of the morphologies of the constituent layers, but also the BL actuator, suggesting the healing capability.

2.3.2. The Healing Performance

Second, we studied the mechanical performance of the BL actuator by performing tensile stretching measurements. The strain–stress curves of the BL actuator before and after the healing treatment are shown in Figure 4b. Benefiting from this successive heating and humidifying treatment, the tensile strength and elongation-at-break of the healed actuator were restored to 82.1% and 87.4% of the pristine film, respectively. The healing efficiency (η) is defined as the proportion of toughness restored relating to the toughness of the non-injured sample. As shown in Figure 4e, the calculated Young's modulus of the BL actuator reached 72.6% of the original value after healing. Hence, the mechanical properties of the healed actuator were comparable to those of the pristine one.

Third, we investigate the recovery of the photo-responsiveness of the actuator after the healing procedure. To demonstrate the actuating and healing functions, an athlete robot was fabricated, which executes sit-up movements in 5 s upon the illumination of UV LED ($\lambda = 375$ nm, $I = 78$ mW cm^{-2}) and lifts up a cargo 16 times heavier than itself. The healed "athlete" resumed its operation and performed the sit-up motion. On the one hand, Figure 4c presents the actuating force generated by a healed BL actuator in response to UV LED illumination, which is 0.22 MPa in the first and second actuation cycles, respectively. No obvious decrease in the average actuation force of the healed actuator compared to that of the pristine one is observed. The calculated healing efficiency in terms of the restoration of the actuating force is 95.6%. On the other hand, Figure 4d and Movie S2 (Supporting Information) compares the time-dependent variation of the bending angle of the original (orange) and healed (green) actuators under the illumination of UV LED. It can be observed that there were no obvious differences in the maximum bending angles (centered at ≈42°) of the two actuators, despite a slight decrease in the speed of response from 8.5 to 7.0°·s^{-1}. The above-mentioned results demonstrate that the healed actuators possess satisfactory structural strength and stimuli-responsiveness, which benefits the durability of the soft actuators in a variety of complex application environments.

2.3.3. New Actuation Functions Through Welding the Actuators

The stimuli-induced structural rearrangement of the two respective layers not only assists in the healing of the microscale injuries for a single BL actuator device, but shape reprogramming of more BL actuator devices by welding. The welding of actuators can be achieved at both the PPC film side with the aid of humid air, and the MCP film side by moderate heating, respectively.

Figure 5a depicts the procedures of welding through the PPC film side (mode 1). A strip of BL actuator is cut by half along the longitude direction, a drop of water is dipped onto the middle of one of strips A at the PPC film side, and strip B is attached onto strip A face-by-face at the PPC film side with a moderate press. The "grafted" actuator is then placed at the ambient condition (T = 25 C, RH = 30%) for 30 min to allow for water evaporation and efficient welding. Similarly, we have successfully welded two separated strips of the BL actuator at the MCP film side (mode 2). The cut strips were heated at 60 °C for 15 min to achieve moderate melting and maintain the intact film. The two separate strips were overlapped face-by-face in the MCP film side at the middle of the strips, and the "grafted" actuator was heated at the same condition for another 15 min. The MCP film part in the two separate strips fused together, and contributed to the formation of a welded actuator when the environmental temperature decreased to 25 °C. The separated strips become firmly fused at the junction site via structural rearrangement of the two stimuli-responsive materials.

The corresponding SEM images at the welding junction sites are shown in Figure 5b,c. In both modes, the welded actuators exhibit uniform morphologies without obvious delamination. Therefore, the BL actuator can be reprogrammed by welding both the PPC films and the MCP films under their specific stimuli. To verify the stability of the fused point and the actuating functions using the welding methods, we studied the time-dependent bending angles of the two welded actuators in response to IR LED illumination (Figure 5d,e). Herein, A refers to the strip at the bottom and B refers to the one at the top in the reprogrammed actuator. For example, the upper surface in strip A, mode 1 of the BL actuator is PPC film. And the upper surface in strip B, mode 1 is MCP film.

The welded actuator can perform diverse actuation functions under the illumination of IR LED. As shown in Figure 5d,e and Movie S3 (Supporting Information), the four arms of the two actuators (modes 1 and 2) are nearly flat before the test. When the actuator (mode 1) is illuminated with the IR LED, the two arms (strip A) are bent upward and the other two arms (strip B) bend downward to 68° ($\tan\theta = 0.83$) in 25 s, respectively (Figure 5f). And when the actuator (mode 2) is irradiated, the two arms in strip A bend downward, and the other two in strip B bend upward to 68° in 23 s, respectively. On the one hand, the bending speed in mode 1 is a little bit slower than that in mode 2 (Figure 5g).

Since the overlapping of the PPC film leads to a decrease in the surface area of the PPC film, from which the water desorption rate might be negatively influenced, and a slower shape deformation speed is obtained. On the other hand, the difference between the bending speed in stripes A and B is higher in mode 2 than in mode 1. This is due to that the distance between the arms of the PPC films in the two strips is larger in mode 2 than 1, so a larger gradient of humidity is achieved. Otherwise, as the case in mode 1, when the two PPC films are close together, the desorbed water creates a higher concentration of moisture surrounding the films, and slows down the shape deformation speed. However, in general, the speed of photo-responsive bending deformation does not decrease compared to the pristine one after the welding procedure.

Through the experiments above, we preliminary demonstrate the basic reprogrammed actuators fabricated by welding of the PPC film and MCP film, respectively. We anticipate that these welding methods can provide new opportunities for fabricating actuators with predesigned shapes and complex shape morphing.

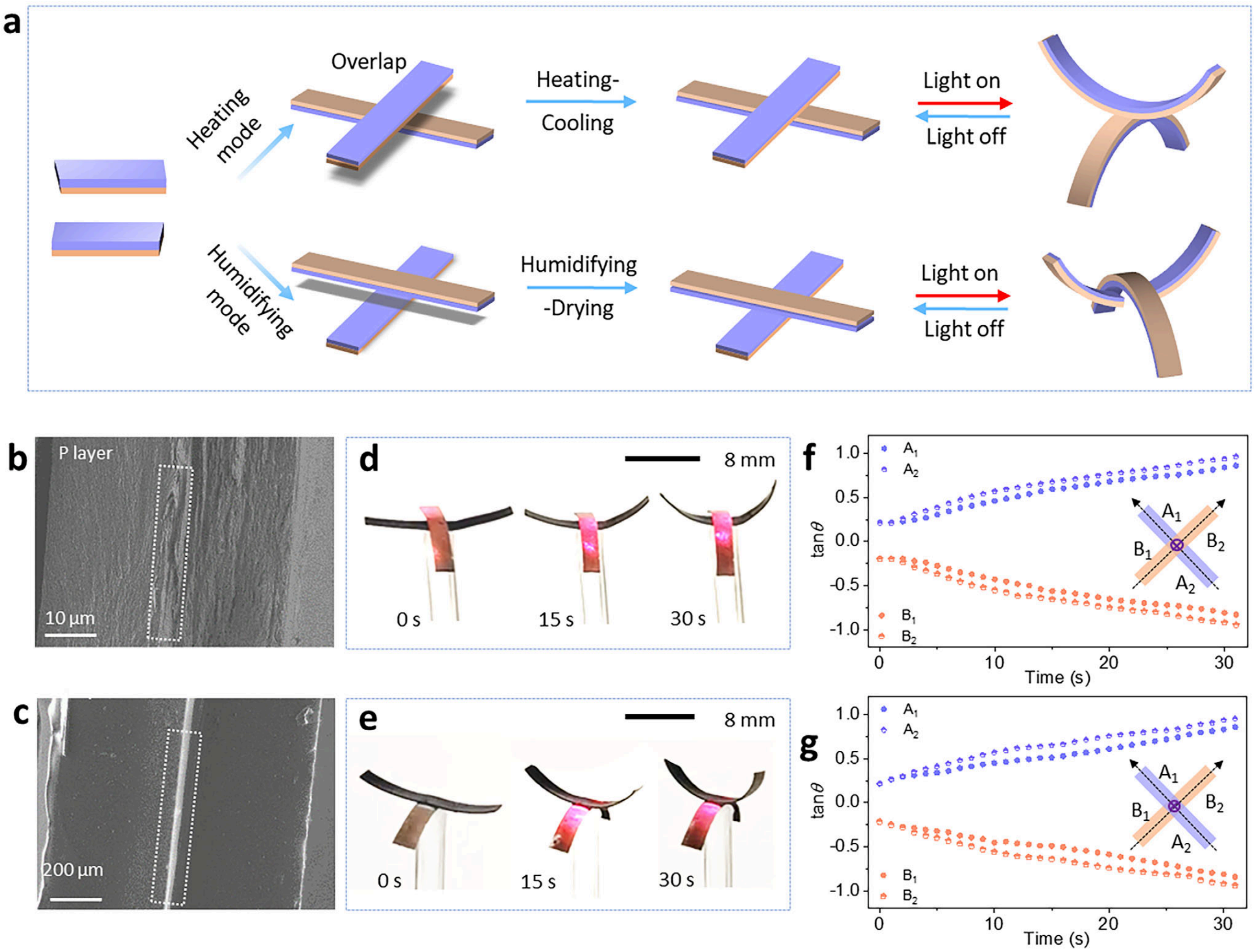

Figure 5. Actuation performance of the welded actuator. a) Schematic diagrams for welding of the BL actuator through the PPC film or the MCP film interfaces. b,c) SEM micrographs showing the welded interface of the M (b) and P (bottom) layers (c), respectively. d,e) Photos recorded during the actuation cycle of reprogrammed BL actuators welded through the MCP film (d) and the PPC film (e). Time-dependent bending angles of the four arms in the welded actuators when illuminated by IR LED, with the Mode 1 actuator in (f) and the Mode 2 actuator in (f), respectively.

3. Discussion

By combining humidity- and photo-responsive materials with complementary properties, we obtained a double-stimuli-responsive BL actuator (**Figure 6**). This work provides an effective strategy for the design of healable and stimuli-responsive materials for robotic applications. This is one of the few reports of an actuator that integrates stimuli-responsive deformation and micro-scale healing performance from the LBL assembly of two structurally reprogrammable materials. The structural rearrangement triggered by environmental stimuli leads to i) the healing function when the actuator is damaged since a higher number of the stimuli-responsive polymer exposed at the fractured surface will result in a lower rate of energy dissipation for reconstructing the polymer network, and ii) the actuating function due to the strain mismatch at the layer interface when the actuator remains intact through the efficient energy absorption/dissipation pathways.[21] Compared to room-temperature healable materials, the softening of our material could be controlled by exposure to external stimuli, which also ensures the mechanical stability and durability of the actuators in ambient conditions.

The as-obtained BL actuator represents a new platform, which can be broadened by incorporating various stimuli-responsive elements that transform the energy inputs of stimuli into actuating or healing functions. Besides, the PPC and MCP films could be exploited as coating or hosting materials for other stimuli-responsive elements for more diverse multi-component systems and soft robotics applications. In this respect, the mechanisms of healing at the material interfaces are a topic of interest for our future studies.

4. Conclusion

In summary, we employed a layer-by-layer casting method to fabricate a healable actuator by integrating two stimuli-responsive materials with compatible and complementary properties, which

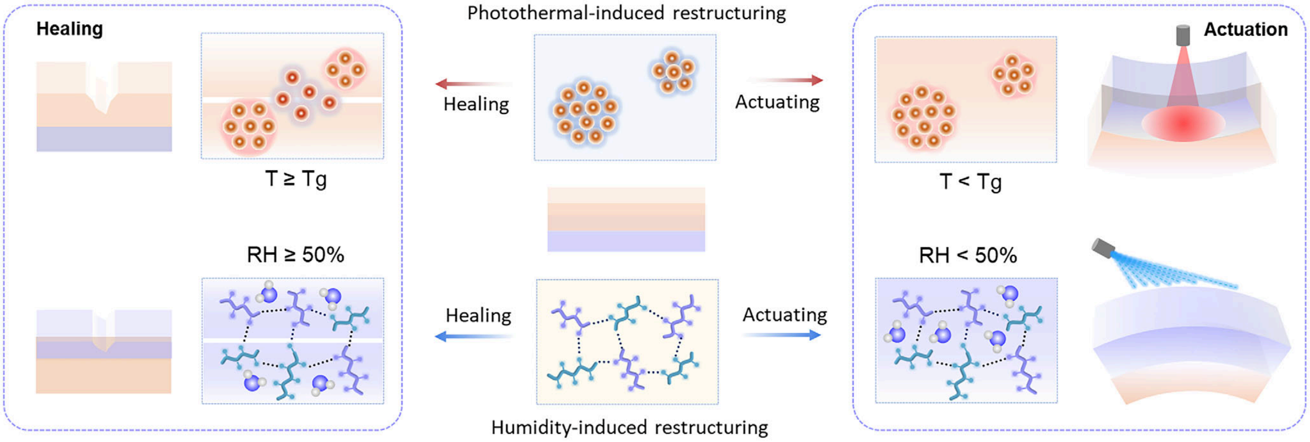

Figure 6. Humidity and thermal-induced actuation and healing of the bi-layered actuator through structural reconfiguration. Actuation deformation mode and self-healing mode of the BL actuator in response to humidity and photo-thermal stimuli. Adapted from.[27]

undergo structural rearrangement induced by a humidifying–drying and a heating–cooling treatment, respectively. Due to the dynamic nature of both materials, they can be activated under certain stimuli, which can lead to either an actuation or microscale healing function depending on the integrity of the respective layer. A powerful actuating strength is achieved when the actuator is illuminated by an infrared LED. Moreover, the punctured actuator, as a whole device can be healed by humidifying–heating–cooling treatment sequentially. In addition, the BL actuator can be reprogrammed by welding two-bisected strips of the actuator, which enables the deformation and change in the dimension of the actuator's shape readily. Welding of the BL actuators produces diverse and multi-mode actuation behavior. Importantly, the healed and welded actuator maintained their actuation performance after these reprogramming methods. Based on these results, we anticipate that this hierarchical actuator holds great promise in different applications wherever programmable structural reconfigurations are needed, such as artificial muscles, soft robotics, or space exploration. Besides, we believe that the layer-by-layer casting strategy will pave a new way for integrating multiple functional materials into novel and intelligent robotics.

5. Experimental Section

Layer-by-Layer Casting: The MCP film was prepared according to the literature.[24] Generally, the prepolymer and curing agent of PDMS, Si-CNC, Fe_3O_4 NP dispersion were mixed at a volume ratio of 2:20:1, poured onto the Petri dish, degassed, and cured at 25 °C for 48 h. The as-obtained MCP film was then treated with oxygen plasma (100 W, 3 min, 5 sccm O_2) to increase hydrophilicity as well as adhesion of the following PPC film, which was obtained by casting of the mixed dispersion of PEDOT:PSS and CMC as described in the previous research.[23]

Fourier Transform Infrared Spectroscopy (FTIR): The FTIR spectra of the PPC and the MCP films were recorded at the ambient condition (T = 25 °C, RH = 30%). The reflectance infrared spectra were collected through a Bruker Vector 22 spectrometer with a diamond cell attenuated total reflection accessory module in the range of 800–4000 cm^{-1}.

Scanning Electron Microscopy: The SEM measurements were performed at the Electron Microscopy Center of Empa. Prior to measuring, the samples were coated with carbon by the Safematic CCU-010 coating machine. The sputtering time was 50 s and the thickness of the coating was 10 nm. The morphology of the welded samples was characterized at a high-resolution scanning electron microscope (Gemini SEM 460, Zeiss, Germany). SEM micrographs were recorded using the SE2 and in-length electron detector at an accelerating voltage of 2.00 kV. The cross-section of the bi-layered actuator was detected by a field-emission scanning electron microscope (FEI Quanta FEC 650, Germany) coupled with an energy-dispersive spectrometer (EDS, Bruker Flat Quad 5060F). The FESEM measurement was carried out at a relatively low accelerating voltage of 0.5 kV with an Everhart-Thornley detector.

Small-Angle X-ray Scattering: The SAXS experiments were carried out at the P03 MiNaXS beamline at the synchrotron source PETRA III at Deutsches Elektronen Synchrotron (DESY), Germany.[28] The experiments were performed at the energy of 11.8 keV with a wavelength of λ = 0.105 nm. The beam size was 80 × 56 µm2 (horizontal × vertical). The sample-detector distance was kept at 9570 ± 5 mm. A Pilatus 2 M detector (Dectris AG, Switzerland) with a pixel size of 172 × 172 µm2 was used for SAXS.

Small-Angle Neutron Scattering: SANS experiments were performed using the Very Small Angle Neutron Scattering (VSANS) instrument BL-14 at the China Spallation Neutron Source (CSNS).[29] Neutron data were collected with a wavelength range from 2.2 to 6.7 Å, employing a collimation length of 12.75 m. Data reduction was performed using the direct beam method which included measurement of the direct beam, solid angle, and transmission correction as well as background subtraction.[29]

Analysis of the Small-Angle Scattering Data: To obtain a quantitative analysis of the structural information, azimuthal cuts of the 2D SAXS and SANS data were made by DPDAK v 1.4.1 software[30] in the indicated region from $q = 0.03\ \text{nm}^{-1}$ to $q = 0.7\ \text{nm}^{-1}$. The calculation of the scattering length density (SLD) values of Fe_3O_4 NP, and Si-CNC/PDMS was conducted by the calculating tool from the website of https://www.ncnr.nist.gov/. All modeling of the SAXS curves was done using SASView v5.0.3 software,[31] which was an open-source analysis software for small-angle scattering data. The χ^2 -values were used as an indicator for evaluating the suitable fits.

Dynamic Vapor Sorption Analysis: Dynamic water vapor adsorption and desorption were measured by an automated sorption balance device (DVS Advantage ET85, Surface Measurement Systems Ltd., USA). Samples of 10 mg were dried for 6 h at 60 °C and at a partial water vapor pressure of $p/p_0 = 0$. The samples were then exposed to ascending p/p_0 from 0 to 0.98 with a step of 0.05 for adsorption and then descending in the same manner for desorption. The samples were exposed to a N_2 flow rate of 200 sccm.

Tensile Test: The mechanical properties of the constituent layers and the bilayer were examined by a Zwick Z005 testing machine. Samples for mechanical stretching were cut with a size of 40 mm × 8 mm (length × width). Three stripes for each sample were tested at the ambient condition

(T = 25 °C, RH = 30%). The bottom clamp was attached to a 50 N load cell. The stretching rate was 10 mm min^{-1}. The average thickness of the PPC, MCP, and the BL films were 40 ± 5 µm, 400 ± 35 µm, and 400 ± 50 µm, respectively. The data was recorded by textXpert II software. For simplicity, only one representative strain–stress curve for each sample is shown in the manuscript. The tensile strength and elongation-at-break were obtained by averaging the values from three strain–stress curves for each sample.

Photo-Responsive Actuation: 1) To quantify the photo-responsive bending deformation of the BL actuator, an IR LED at a wavelength of 780 nm and a current density of 0 to 89 mW cm^{-2} was used in the ambient condition (T = 25 °C, RH = 30%). The BL actuator (width × length: 5 mm × 20 mm) was held by a clamp, and the free end of the sample was irradiated by an IR LED until the bending angle reached the maximum, and the LED was then switched off. The bending angle, bending radii, and curvature were recorded by a video camera. At least three videos were taken to obtain the parameters for analysis by Origin v2022 software. 2) To quantify the photo-responsive actuation strength of the BL actuator, a Zwick Z005 testing machine was used. The data was recorded by textXpert II software. The BL actuators (width × length: 5 mm × 20 mm) were stretched straight at RH = 80% and fixed between the two holders of the testing machine. The middle part of the actuator was irradiated by an IR LED (780 nm, 89 mW cm^{-2}) for 60 s to generate a contractile force. Then the LED was switched off, and the actuator was gradually cooled down by environmental humidity for 62 s. Three samples were tested for measuring the light-induced internal stress, and each of the measurements on each sample was repeated for 5 cycles.

Infrared Imaging: Temperature profiles on the BL actuators were captured by an infrared camera (ImageIR 8300 hp, Infratec AG.). The radiation detector was an InSb quantum detector that was sensitive in the 2–5.7 µm wavelength range. During the measurements, the IR camera recorded up to 200 frames per second with a resolution of 640 × 512 pixels at 0.149 mm per pixel. The samples with a size of (width × length: 8 mm × 20 mm) were fixed by two clamps and irradiated by LEDs with different wavelengths at the same current density of 89 mW cm^{-2} until reaching their maximum temperature, and the LED was then switched off. The mountable LEDs were purchased from Thorlabs GmbH, Germany. The IR camera was used to record the temperature variation during this process. The highest temperature was obtained under the illumination of IR LED (wavelength 780 nm). Therefore, the temperature of the samples was further measured under IR LED at an increasing power density (2.5, 7.8, 13.4, 38, 68, and 89 mW cm^{-2}).

Healing of the BL Actuator: The humidity- and heating-induced healing of the PPC and the MCP films was observed under an optical microscope (ZEISS SteREO Discovery.V20) with a 40 × objective. An "athlete" robot was fabricated by cutting a BL actuator into a rectangular shape (width × length: 8 mm × 20 mm, 15 mg). A non-stimuli-responsive cargo (240 mg) was attached to one side of the robot by coating a thin-layer of 10 µL glue on the film surface. A needle was used to make a puncture through the actuator with a diameter of injury of 500 µm. The actuator was first heated at 60 °C for 0.5 h, and then subjected to a humid environment with RH of 70% for 0.5 h to heal.

Welding of the BL Actuators: The two welded actuators were prepared as follows: two strips of the BL actuators (width × length: 8 mm × 25 mm) were cut along the longitude direction. For mode 1: two pieces of the cut actuator were overlapped in the middle with PPC films at the interface with the aid of a drop of water. After staying 0.5 h at the ambient condition, the welded actuator was obtained. For mode 2: the other two pieces of the cut actuators were overlapped in the middle with the PPC films facing each other under moderate heating (60 °C) for 0.5 h to obtain the welded actuator.

Calculation of Healing Efficiency: The healing efficiency (η) of the Bl actuator was calculated in terms of the restoration of their maximum strength (σ), where σ_{healed} and $\sigma_{pristine}$ represent the maximum strength of the sample after healing and their pristine counterpart.

$$\eta = \frac{\sigma_{healed}}{\sigma_{pristine}} \times 100\% \tag{1}$$

$$\eta = \frac{\theta_{healed}}{\theta_{pristine}} \times 100\% \tag{2}$$

The healing efficiency of the BL actuator was described by the restoration of its maximum bending angle (θ), where κ_{healed} and $\kappa_{pristine}$ represent the maximum curvature of the actuator after healing and its pristine counterpart.

Supporting Information

Supporting Information is available from the Wiley Online Library or from the author.

Acknowledgements

This research was at large funded by the European Union's Horizon 2020 research and innovation programme under grant agreement No. 964388 as COgITOR: A new COlloidal cyberneticIc sysTem tOwaRds 2030. The authors acknowledge Prof. Frank Nüesch (Empa Laboratory of Functional Polymers) for giving access to the FTIR measurement, and Dr. Robin Pauer (Empa Electron Microscopy Center) for their support in the SEM experiments. Qing Chen acknowledge the funding of the Very Small Angle Neutron Scattering Instrument Project, supported by the Department of Science and Technology of Guangdong Province, Guangdong Natural Science Foundation, National Natural Science Foundation of China (grant No. 22273046). The authors thank the staff members of the Very Small Angle Neutron Scattering at the China Spallation Neutron Source (CSNS) (https://cstr.cn/31113.02.CSNS.VSANS), for providing technical support and assistance in data collection and analysis. The authors acknowledge DESY (Hamburg, Germany), a member of the Helmholtz Association HGF, for the provision of experimental facilities. Parts of this research were carried out at the P03 beamline and the authors would like to thank Dr. Matthias Schwartzkopf and Dr. Andrei Chumakov for assistance in preparing the beamline for SAXS measurements. The authors are thanking Matteo Bevione (Empa) for assistance with SAXS data acquisition. The authors acknowledge Prof. He Cheng, Dr. Changli Ma, and Dr. Taisen Zuo for assistance with SANS data acquisition at CSNS.

Conflict of Interest

The authors declare no conflict of interest.

Data Availability Statement

The data that support the findings of this study are available from the corresponding author upon reasonable request.

Keywords

healing, layer-by-layer casting, stimuli-responsive actuator, structural rearrangement, welding

Received: March 27, 2025
Revised: May 5, 2025
Published online: June 3, 2025

---

[1] W. Wagermaier, K. Razghandi, P. Fratzl, *Adv. Mater.* **2025**, 2413096.

[2] a) Z. Madani, P. E. S. Silva, H. Baniasadi, M. Vaara, S. Das, J. C. Arias, J. Seppala, Z. Sun, J. Vapaavuori, *Adv. Mater.* **2024**, *36*, 2405917; b) Q. Chen, B. Sochor, A. Chumakov, M. Betker, N. M. Ulrich, M. E. Toimil-Molares, K. Gordeyeva, L. D. Söderberg, S. V. Roth, *Adv. Funct. Mater.* **2022**, *32*, 2208074.

[3] G. D. Zhu, Y. Hou, N. Xia, X. Wang, C. Zhang, J. Z. Zheng, D. D. Jin, L. Zhang, *Adv. Funct. Mater.* **2023**, *33*, 2300888.
[4] Z. Wang, N. M. Freris, X. Wei, *Device* **2025**, *3*, 100646.
[5] H.-V. Phan, D. Floreano, *Sci. Robot.* **2024**, *9*, ado3890.
[6] D. B. H. Min, S. Jang, S. Lee, M. Park, C. B. Dayan, J. Choi, K. Bak, Y. Yang, M. S. S. Chun, *Sci. Adv.* **2024**, *10*, adp8260.
[7] Y. Qu, W. Tang, Y. Zhong, Q. Sheng, H. Xu, K. Qin, Z. Li, X. Guo, Y. Gao, H. Yang, J. Zou, *Adv. Mater.* **2024**, *36*, 2403954.
[8] I. Roppolo, M. Caprioli, C. F. Pirri, S. Magdassi, *Adv. Mater.* **2024**, *36*, 2305537.
[9] T. Yimyai, A. Pena-Francesch, D. Crespy, *Macromol. Rapid Commun.* **2022**, *43*, 2200554.
[10] C. Takahashi, M. Giuliani, B. Lennox, W. R. Hamel, R. Stolkin, C. Semini, *Front. Robot. AI* **2021**, *8*, 744092.
[11] M. W. M. Tan, H. Bark, G. Thangavel, X. Gong, P. S. Lee, *Nat. Commun.* **2022**, *13*, 6769.
[12] Z. Huang, Z. Wu, C. Li, X. Li, X. Yang, X. Qiu, Y. Wang, Y. Miao, X. Zhang, *Adv. Mater.* **2025**, *37*, 2413194.
[13] Z. Cui, Y. Zhang, N. Li, Z.-H. Ren, Z.-H. Guan, *Mater. Today Chem.* **2024**, *42*, 102427.
[14] S. Zhang, Z. Wang, J. Zhang, J. Liu, C. Sun, S. Qin, Y. Ren, L. Zhang, W. Hu, H. Yang, *Chem. Eng. J.* **2024**, *491*, 152185.
[15] N. Wang, X. Yang, X. Zhang, *Nat. Commun.* **2023**, *14*, 814.
[16] J. von Szczepanski, P. M. Danner, D. M. Opris, *Adv. Sci.* **2022**, *9*, 2202153.
[17] J. Lin, P. D. Zhou, Q. H. Chen, W. Zhang, Z. L. Luo, L. Z. Chen, *Sens. Actuator B: Chem.* **2022**, *362*, 131776.
[18] R. Q. Yuan, G. Lu, N. Yang, D. You, J. R. Wang, Q. L. Zhang, Q. Cheng, L. Q. Ge, *Chem. Eng. J.* **2022**, *434*, 134212.
[19] Y. Yang, H. M. Wang, S. Zhang, Y. Wei, X. M. He, J. L. Wang, Y. Y. Zhang, Y. Ji, *Matter* **2021**, *4*, 3354.
[20] C. C. Kim, A. R. Ramaswami, R. F. Shepherd, *Adv. Mater.* **2025**, *37*, 2414872.
[21] X. Yan, Q. Chen, Z. Huo, N. Zhang, M. Ma, *ACS Appl. Mater. Interfaces* **2022**, *14*, 13768.
[22] a) J. J. Richardson, M. Bjornmalm, F. Caruso, *Science* **2015**, *348*, aaa2491; b) Y. Hamzat, A. A. A. Aljabali, M. El-Tanani, M. M. Tambuwala, *Curr. Nanosci.* **2025**, *21*, 404.
[23] Q. Chen, T. Künniger, Q. Song, K. Zhang, A. Chumakov, Y. Bulut, C. Harder, P. Müller-Buschbaum, S. V. Roth, A. Braun, *Adv. Funct. Mater.* **2024**, *34*, 2402924.
[24] Q. Chen, R. Furrer, L. Jamilpanah, A. Chumakov, Y. Bulut, C. Harder, P. Müller-Buschbaum, S. V. Roth, A. Braun, *ACS Nano* **2025**, *19*, 6165.
[25] B. E. Schubert, D. Floreano, *RSC Adv.* **2013**, *3*, 24671.
[26] R. H. Baughman, *Science* **2005**, *308*, 63.
[27] Q. Chen, *J. Mater. Res.* **2024**, *39*, 2349.
[28] A. Buffet, A. Rothkirch, R. Döhrmann, V. Körstgens, M. M. A. Kashem, J. Perlich, G. Herzog, M. Schwartzkopf, R. Gehrke, P. Müller-Buschbaum, S. V. Roth, *J. Synchrotron Radiat.* **2012**, *19*, 647.
[29] T. Zuo, Z. Han, C. Ma, S. Xiao, X. Lin, Y. Li, F. Wang, Y. He, Z. He, J. Zhang, G. Wang, H. Cheng, *J. Appl. Crystallogr.* **2024**, *57*, 380.
[30] G. Benecke, W. Wagermaier, C. Li, M. Schwartzkopf, G. Flucke, R. Hoerth, I. Zizak, M. Burghammer, E. Metwalli, P. Müller-Buschbaum, M. Trebbin, S. Förster, O. Paris, S. V. Roth, P. Fratzl, *J Appl. Crystallogr.* **2014**, *47*, 1797.
[31] M. Doucet, J. H. Cho, G. Alina, Z. Attala, J. Bakker, W. Bouwman, P. Butler, K. Campbell, T. Cooper-Benun, C. Durniak, L. Forster, M. Gonzales, R. Heenan, A. Jackson, S. King, P. Kienzle, J. Krzywon, T. Nielsen, L. O'Driscoll, W. Potrzebowski, S. Prescott, R. F. Leal, P. Rozycko, T. Snow, A. Washington, *Zenodo* **2020**.